

Vacillations in a Shallow-Water Model of the Stratosphere

PING-PING RONG AND DARRYN W. WAUGH

Department of Earth and Planetary Sciences, Johns Hopkins University, Baltimore, Maryland

(Manuscript received 29 September 2003, in final form 19 December 2003)

ABSTRACT

The evolution of the polar vortex in a shallow-water model with time-independent topographic forcing and relaxation to a constant equilibrium state is investigated for a range of topographic forcing amplitudes. For small forcing amplitudes there are only weak disturbances on the edge of the polar vortex and the vortex area remains constant, whereas for large amplitudes there are cycles where the vortex breaks down and then reforms (and zonal winds vacillate between westerlies and easterlies). Analysis of the mass within potential vorticity (PV) contours shows that these vacillations are due to out-of-phase variations in the mass fluxes across PV contours due to the relaxation and to hyperdiffusion. During the strong vortex stages Rossby wave breaking produces a cascade of PV to small scales, and these small-scale features are eventually eliminated by hyperdiffusion. This causes a decrease in the mass within the high PV contours and ultimately the destruction of the vortex. In contrast, during stages with no vortex there are very weak PV gradients, weak Rossby wave activity, and little cascade of PV to small scales. The vortex, and PV gradients, are then reestablished by the mass fluxes due to the diabatic relaxation term. These results suggest that the horizontal PV structure may play an important role in the vortex breakdown and recovery in three-dimensional models and in the real stratosphere.

1. Introduction

In recent years there has been a great deal of interest in the variability in the stratosphere–troposphere system, and the possibility that the stratosphere may influence the modes of variability in the troposphere. In particular, several studies have shown a link between the strength of stratospheric wintertime polar vortices and surface climate and weather (e.g., Thompson and Wallace 1998; Baldwin and Dunkerton 1999, 2001; Thompson et al. 2002). This has renewed interest in internal modes of variability within the stratosphere and the possibility that the cycles in the breakdown and recovery of the polar vortices, which influence the troposphere, could be due to processes internal to the stratosphere.

There is a long history of modeling studies showing that the stratosphere has its own modes of internal variability (e.g., Holton and Mass 1976; Schoeberl and Strobel 1980; Yoden 1987; Christiansen 1999; Scott and Haynes 2000). In these studies it was shown that variability in the stratosphere, in particular vacillations between westerlies and easterlies, can occur even when the wave forcing at the bottom of the model is time independent. In these models (and in the real stratosphere) the breakup of the polar vortex, and the transition of westerlies to easterlies, occurs first in upper

levels and then migrates down through stratosphere. The interpretation of the vacillations in the majority of the above studies was in terms of the transition to easterlies leading to the formation of critical lines, which prevent further upward propagation of the planetary waves and allow the upper levels of the vortex to redevelop via thermal processes.

Here we examine the internal variability within a single-layer shallow-water model of the stratosphere with time-independent topographic forcing. Although previous studies have used single layer models to examine a variety of aspects of stratospheric dynamics (e.g., Jukes and McIntyre 1987; Jukes 1989; Salby et al. 1990; O’Sullivan and Salby 1990; Waugh 1993; Yoden and Ishioka 1993; Norton 1994; Polvani et al. 1995; Sobel and Plumb 1999; Thuburn and Lagneau 1999), we are unaware of any studies documenting and examining the internal variability in such models. Our calculations show that for large amplitude topographic forcing there are cycles in which the vortex breaks down and then rebuilds, and correspondingly the winds at high latitudes vacillate between westerlies and easterlies. The existence of vacillations in a single layer model means that deep vertical structure and the above vertical shielding mechanism are not necessary for breakdown and recovery cycles of polar vortices and that horizontal aspects of the flow may also be important.

The shallow water model and diagnostics used are described in the next section. The main results are presented and discussed in section 3, while sensitivity ex-

Corresponding author address: Dr. Darryn Waugh, Department of Earth and Planetary Sciences, Johns Hopkins University, 3400 N. Charles St., Baltimore, MD 21218.
E-mail: waugh@jhu.edu

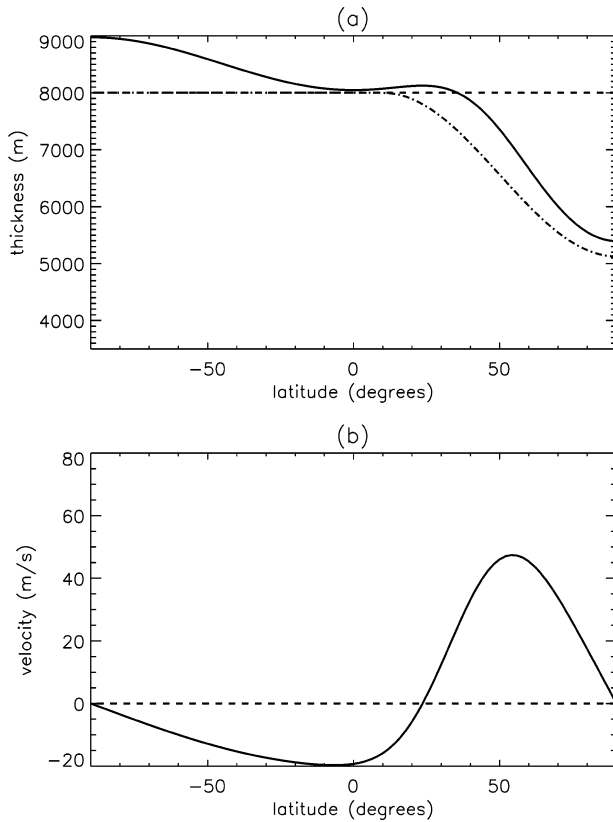


FIG. 1. Latitudinal variation of (a) height and (b) zonal winds for initial conditions (solid curves). The variation of the equilibrium height field h_E is also shown in (a) (dot-dashed curve).

periments are briefly discussed in section 4. Concluding remarks are in section 5.

2. Model and diagnostics

a. Model equations

The shallow-water model used is the same as in Polvani et al. (1995) and Sobel and Plumb (1999). The model equations are

$$\zeta_t = -\nabla \cdot (\mathbf{v}\zeta_a) + G, \quad (1)$$

$$\delta_t = -\frac{1}{2}\nabla^2(\mathbf{v} \cdot \mathbf{v}) + \mathbf{k} \cdot \nabla \times (\mathbf{v}\zeta_a) - g\nabla^2(h + h_B), \quad (2)$$

$$h_t = -\nabla \cdot (h\mathbf{v}) + H, \quad (3)$$

where relative vorticity ζ , divergence δ , and thickness h are the prognostic variables: $\zeta_a = \zeta + f$ is the absolute vorticity (f is the Coriolis parameter); $\mathbf{v} = (u, v)$ is the velocity; h_B is the height of the bottom topography; H represents a mass source; and G dissipation of vorticity. The mass source is given by

$$H = (h_E - h)/\tau_E, \quad (4)$$

where $h_E(\phi)$ is a prescribed zonally symmetric equilibrium height field (dot-dashed curve in Fig. 1a). This

relaxation is used as a crude model of radiative relaxation, and h_E represents the radiative equilibrium state.

The spectral transform method is used to numerically solve the equations, and the dissipation term is scale-selective sixth-order hyperdiffusion; that is,

$$G = \nu \nabla^6 \zeta, \quad (5)$$

where ν is the hyperdiffusion coefficient. The majority of calculations presented here use T42 truncation with $\nu = 5 \times 10^{26} \text{ m}^6 \text{ s}^{-1}$, which corresponds to damping time of around 5 h for total wavenumber 42. However, calculations have been performed at T85 truncation with ν 50 times smaller ($1 \times 10^{25} \text{ m}^6 \text{ s}^{-1}$).

The topography h_B used is of the form

$$h_B = H_B(1 - e^{-t/\tau_B}) \cos(\lambda) e^{[(\phi - \phi_0)/\Delta\phi]^2}, \quad (6)$$

where H_B is the amplitude of the topography, $\tau_B = 5$ days, and the topography is confined latitudinally within a channel of $\Delta\phi = 14.14^\circ$ (half-amplitude width of 2760 km) centered at $\phi_0 = 45^\circ$. These values are approximately the same as used by Polvani et al. (1995). In the calculations presented below, H_B varies between 1000 and 3000 m (undisturbed thickness $h_0 = 8000$ m).

All simulations use the same zonally symmetric initial conditions (Fig. 1). This initial flow is the same as used in Polvani et al. (1995) and is characteristic of the winter middle stratosphere. There is a westerly jet of 50 m s^{-1} at 55°N , a zero wind line around 23°N , and weak easterlies at the equator and in the Southern Hemisphere.

b. Diagnostics

The simulations are examined in terms of zonal mean quantities and budgets as well as potential vorticity (PV) based Lagrangian diagnostics.

The zonal mean zonal momentum equation of the shallow-water system may be written as (Thuburn and Lagneau 1999)

$$\begin{aligned} \bar{u}_t - \bar{v}^* \zeta_a = & \frac{1}{h \cos\phi} \nabla \cdot \mathbf{F} - \frac{g \overline{h h_{B\lambda}}}{a h \cos\phi} - \frac{1}{h} \overline{(h' u')}, \\ & + \frac{1}{h} \overline{u' H'} + \bar{X}^*, \end{aligned} \quad (7)$$

where $\nabla \cdot \mathbf{F} = [1/(a \cos\phi)](F^{(\phi)} \cos\phi)_\phi$ and $F^{(\phi)} = -(\overline{h v})' u' \cos\phi$ is the shallow-water version of the Eliassen–Palm flux. Here an overbar represents zonal mean, a prime departure from the zonal mean, and asterisk and overbar the mass-weighted zonal mean: $h_{B\lambda}$ is the derivative of bottom topography along the zonal direction, and X represents the nonconservative forcing contributed by the hyperdiffusion.

In the calculations examined below the last three terms on the right-hand side of Eq. (7) are small compared with the others, and the zonal wind tendency is a balance between the advection of absolute vorticity by the mean meridional flow and the net convergence of the eddy transport of momentum [where, following

Thuburn and Lagneau (1999), the topographic term is interpreted as the convergence of the vertical eddy transport]. As pointed out by Thuburn and Lagneau (1999), Eq. (7) is the shallow water analog of the transformed Eulerian mean zonal momentum equation in isentropic coordinates for a three-dimensional atmosphere (Andrews et al. 1987).

As the flow is often far from zonal symmetry, the above Eulerian diagnostics can be hard to interpret. It is therefore advantageous to use Lagrangian diagnostics. We consider here several diagnostics that are based on the PV distribution. The PV of the system (1)–(3) is $q = \zeta_a/h$, with governing equation

$$\frac{dq}{dt} = \frac{G - Hq}{h}, \quad (8)$$

where G and H are defined in Eqs. (5) and (4).

A common way to diagnose the evolution of polar vortices, both from meteorological analyses and numerical simulations, is to calculate the area enclosed by PV contours. This area is usually expressed as an equivalent latitude $\phi_E(q) = \sin^{-1}[1 - A(q)/(2\pi a^2)]$, where $A(q)$ is the area of the PV contour and a the radius of the earth. Together with the equivalent latitude, we use a measure of the strength of the jet surrounding the vortex to describe the vortex evolution. The horizontal wind speed is averaged along each PV contour, and the maximum value is defined as the jet strength u_{jet} .

We also use PV contours to calculate modified Lagrangian mean (MLM) diagnostics of the flow (Sobel and Plumb 1999; Thuburn and Lagneau 1999; Neu 2002). The mass within the PV = q contour is given by

$$M(q, t) = \int_{\text{PV}>q} h(q, t) dA, \quad (9)$$

where dA is the area element in the spherical coordinates. Combining this with Eq. (8) the mass tendency can be expressed as (Sobel and Plumb 1999; Thuburn and Lagneau 1999; Neu 2002)

$$\frac{\partial M}{\partial t} = \int \frac{G}{|\nabla q|} dl - q \int \frac{H}{|\nabla q|} dl + \iint_{\text{PV}>q} H dA. \quad (10)$$

The first term on the right-hand side corresponds to the mass flux across the contour due to hyperdiffusion, the second to the mass flux across the contour due to diabatic processes, and the final term to the mass source/sink within (north of) the contour. In the calculations examined below the area integral of mass sink over the vortex is small compared to the other two terms, and the change in mass is a balance between the diabatic and hyperdiffusion mass fluxes.

3. Results

We examine here a series of calculations with relaxation time $\tau_E = 10$ days and topographic forcing am-

plitude H_B between 1000 and 3000 m. Figure 2 shows the temporal evolution of the equivalent latitudes of PV contours, $\phi_E(q)$, together with the jet strength, u_{jet} , for six different H_B . The thick solid curves show the equivalent latitude of the PV = $2.2 \times 10^{-8} \text{ m}^{-1} \text{ s}^{-1}$ contour, which lies within the vortex edge region. Comparison of the different panels shows that the general characteristics of the flow varies as H_B is increased, with a dramatic change around $H_B = 2000$ m. For $H_B < 2000$ m the vortex area and the u_{jet} remain roughly steady after the initial (50 day) adjustment period. However, for $H_B \geq 2000$ m there are periods when the vortex is severely disrupted and decreases in size. For $H_B = 2000$ to 2500 m this vortex disruption occurs intermittently, but for $H_B = 3000$ m there are roughly periodic cycles of high PV loss and deceleration of u_{jet} followed by recovery of high PV and acceleration of u_{jet} .

Although the vortex area is roughly constant for $H_B < 2000$ m, there are still large-scale disturbances along the vortex edge (see Fig. 3a). For larger amplitude the disruption of the vortex is more severe, and the vortex core breaks up and reforms (Figs. 3b,c). For $H_B = 3000$ m, the high PV remnants are completely destroyed before a new vortex core rebuilds.

We now examine in more detail the $H_B = 3000$ m calculation, which shows the clearest and most dramatic vortex breakdown–recovery cycles. We first examine the relative roles of the topographic forcing and relaxation during these cycles using a zonal mean framework. Figure 4 shows the zonal mean zonal wind \bar{u} and the dominant terms in the zonal momentum equation (7). As expected from the plot of $\phi_E(q)$ and u_{jet} (Fig. 2f), \bar{u} shows four distinct cycles of westerlies and easterlies at high latitudes, corresponding to the vortex formation and breakdown. The cycles are not as clear in wind tendency \bar{u}_t (Fig. 4b). However cycles of deceleration and acceleration can be seen, with the periods of acceleration coincident with the vortex rebuilding states, and there is a phase shift of between 20 and 40 days between periods of acceleration and those with strongest westerly winds.

The bottom three panels of Fig. 4 show $\bar{v}^* \bar{\zeta}_a$, the divergence of the horizontal momentum flux $\nabla \cdot \mathbf{F}/(\bar{h} \cos \phi)$, and the topographic forcing term $-g \bar{h} \bar{h}_{BA}/(a \bar{h} \cos \phi)$. The sum of these three terms matches \bar{u}_t very closely (not shown). In midlatitudes, the topography term and horizontal momentum flux oppose each other, and it is the small residual of these two terms, which approximately equals the horizontal PV eddy flux $\bar{h} \bar{v} \bar{q}^*$ (Thuburn and Lagneau 1999), that acts to reduce the zonal wind. Although the topographic forcing initiates the deceleration of \bar{u} this is largely compensated by $\bar{v}^* \bar{\zeta}_a$ (Coriolis torque) and the horizontal momentum flux (which is approximately the relative vorticity flux).

Each term is relatively constant with time, and the cycles in \bar{u}_t (and hence in u) are due to subtle changes in the balance between these terms. Careful examination of Figs. 4c–e shows that there are similar cycles in the

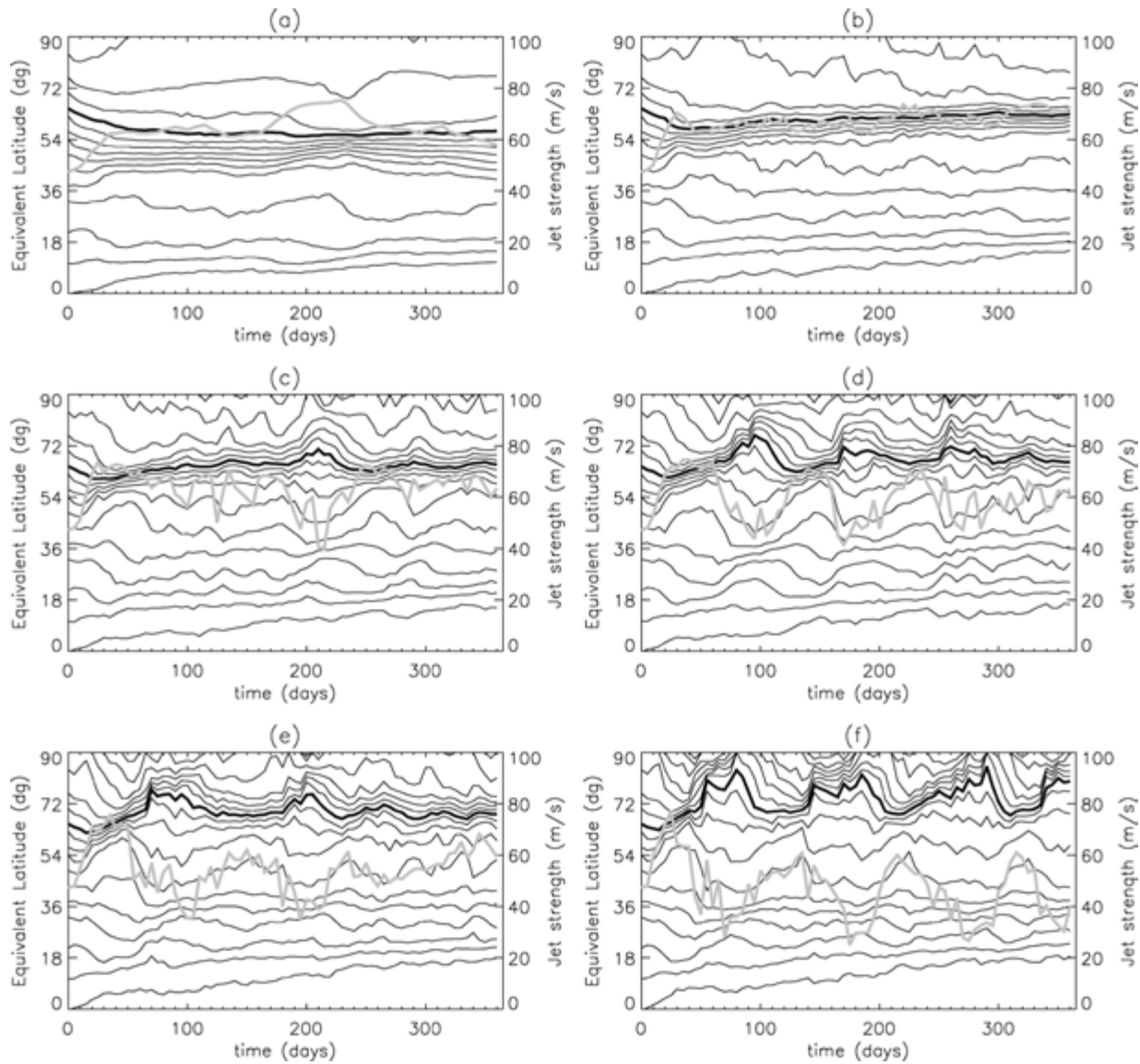


FIG. 2. Temporal evolution of equivalent latitudes $\phi_E(q)$ (black curves) and u_{jet} (gray curves) for calculations with $\tau_E = 10$ days and $H_b =$ (a) 1000, (b) 1500, (c) 2000, (d) 2250, (e) 2500, and (f) 3000 m. Equivalent latitudes ϕ_E are shown for PV at intervals of $0.25 \times 10^{-8} \text{ m}^{-1} \text{ s}^{-1}$ with bold curves corresponding to $q = 2.5 \times 10^{-8} \text{ m}^{-1} \text{ s}^{-1}$.

magnitude of all three terms around 60°N . The magnitude of the horizontal momentum flux and topography term are at a minimum, and $\bar{v}^* \zeta_a$ at a maximum around the periods with easterlies at high latitudes (weak vortex), for example, around days 60, 170, and 280.

We now examine this calculation using the MLM framework. Figure 5a shows the temporal evolution of mass within PV contours. As in the equivalent latitude plot (Fig. 2f), the mass within contours shows four cycles of vortex breakdown and recovery. (Note, for easier comparison with Fig. 2, the mass in Fig. 5a is plotted with decreasing values on the y axis.) The contributions to the change in mass of a PV contour in the vortex edge (thick curve in Fig. 5a) from each of the terms

on the right-hand side of Eq. (10) are shown in Fig. 5b, and the sum of the three terms is shown in Fig. 5c. Figure 5b shows that the mass source/sink within the vortex makes only a minor contribution, and the major balance is between the mass flux across the contour due to diabatic forcing (which increases the mass) and that due to the hyperdiffusion (which decreases the mass). These two mass fluxes are roughly out of phase; that is, when the mass flux due to diabatic forcing is large, the flux due to hyperdiffusion is small. The shaded regions in Fig. 5c show the stages when hyperdiffusion exceeds the diabatic forcing, and match the stages in the upper panel when there is rapid decrease in the mass, that is, stages when the vortex breaks up. Similarly, the

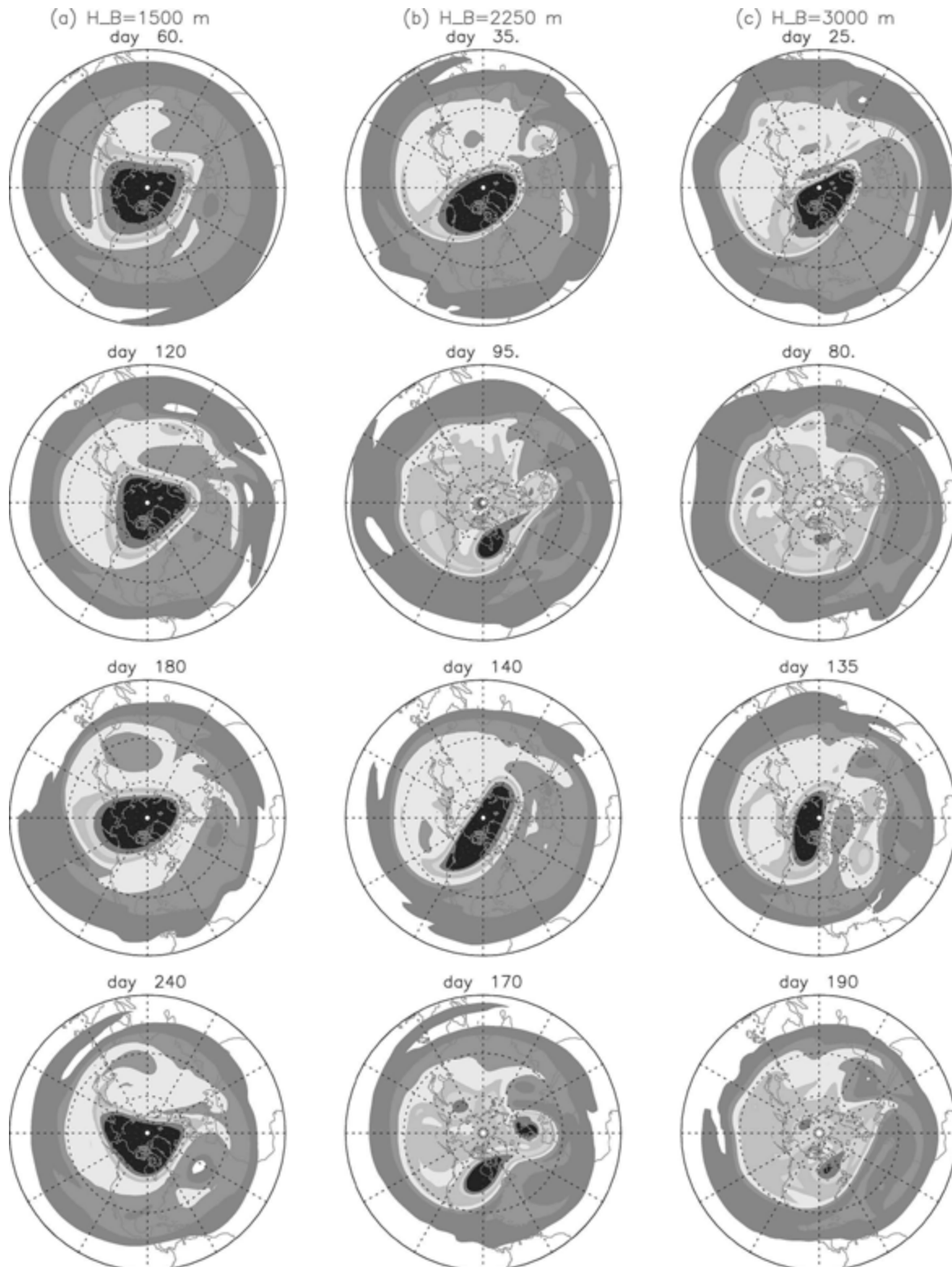


FIG. 3. Polar stereographic maps of PV for calculations with $H_B =$ (a) 1500, (b) 2250, and (c) 3000 m at times shown. The darkest shade inside the vortex corresponds to $q = 3 \times 10^{-8} \text{ m}^{-1} \text{ s}^{-1}$, lightest shading in the surf zone to $q = 1.5 \times 10^{-8} \text{ m}^{-1} \text{ s}^{-1}$, and exterior contour is $q = 0.5 \times 10^{-8} \text{ m}^{-1} \text{ s}^{-1}$.

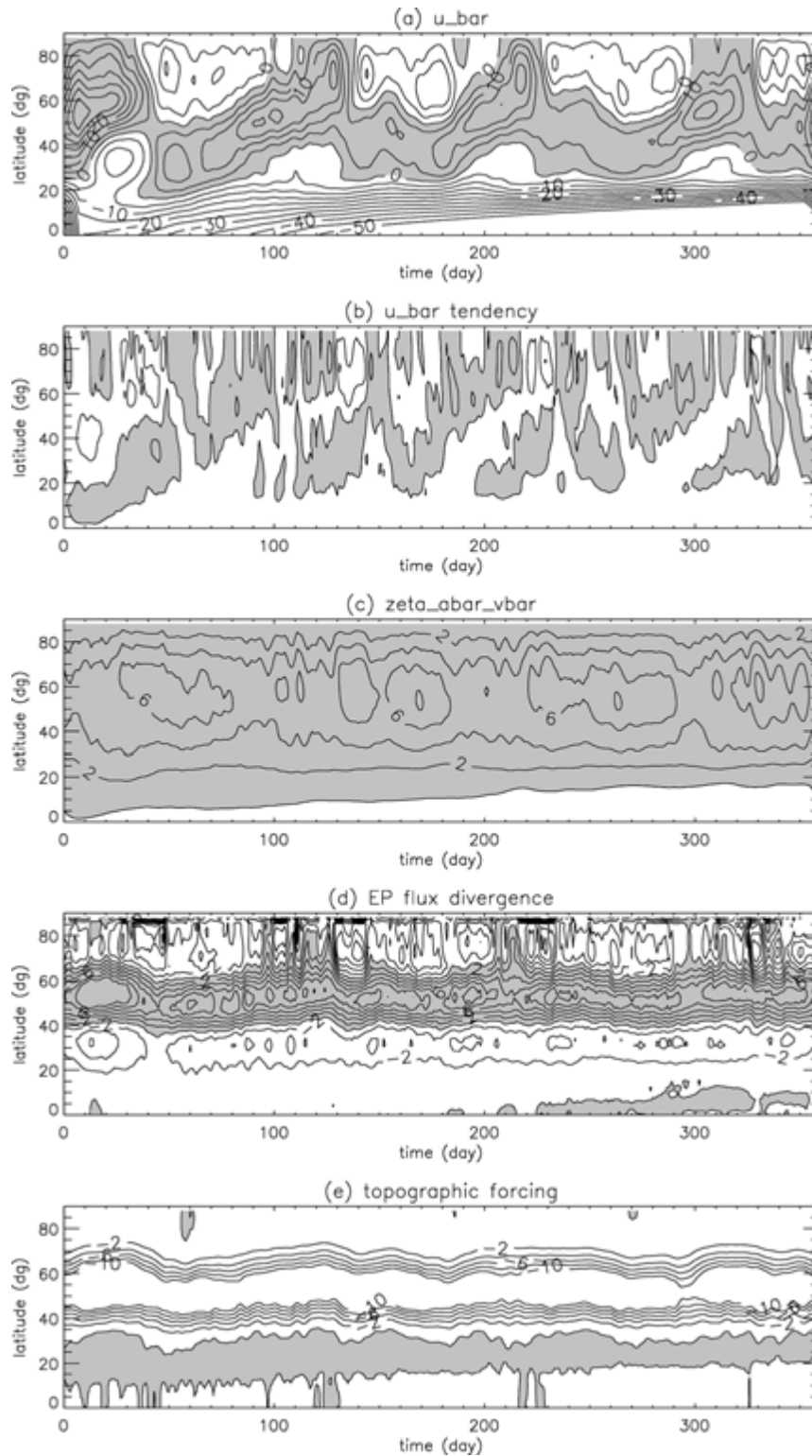


FIG. 4. Time-latitude variations of (a) \bar{u} , (b) \bar{u}_t , (c) \bar{v}_t^* , (d) $\nabla \cdot \mathbf{F}/(\bar{h} \cos \phi)$, and (e) $-g\bar{h}_x/\bar{h} \cos \phi$. Contour interval is (a) 5 m s^{-1} , and (b)–(c) 2 m s^{-2} , with positive values shaded. Contours for winds less than -60 m s^{-1} are not plotted in (a). A 15-day smoothing has been applied to fields in (b)–(e).

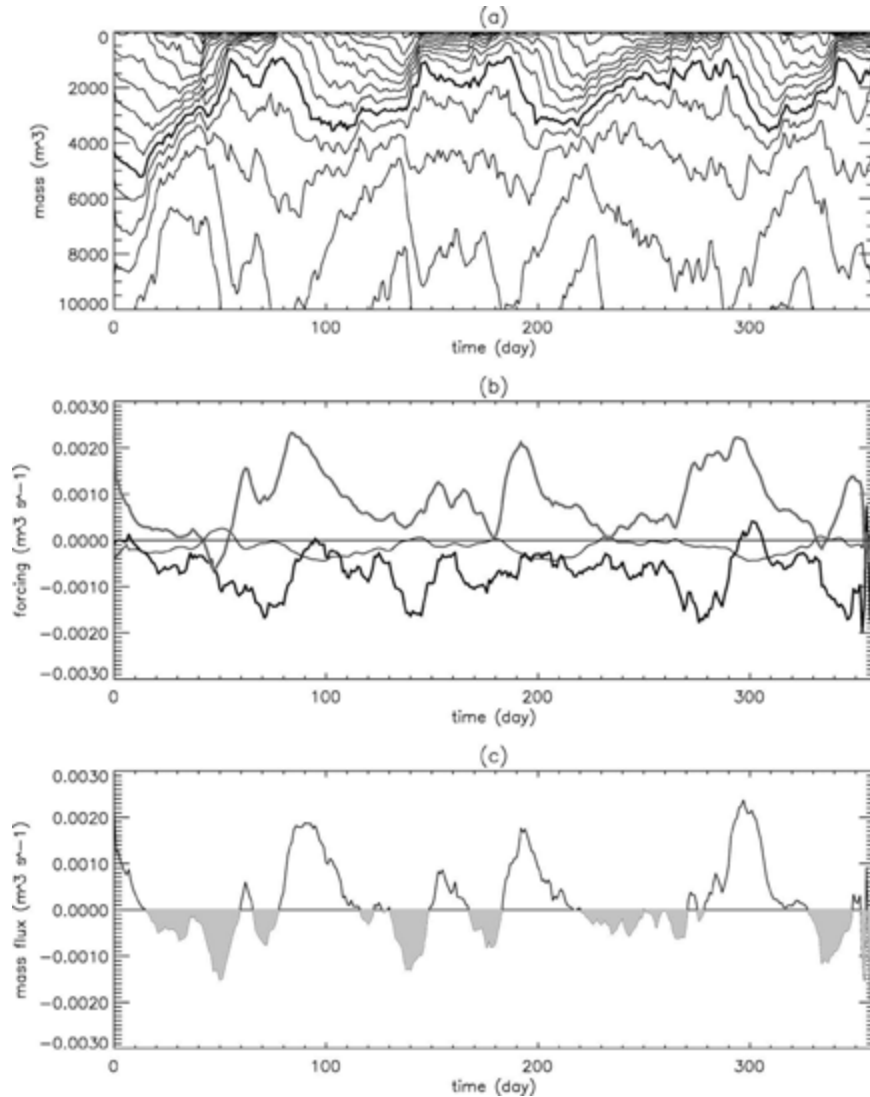


FIG. 5. Mass budget for the $H_b = 3000$ m calculation. (a) Temporal evolution of the mass enclosed by PV contours, for $q = 0, 0.1, \dots, 4.9$, and $5.0 \times 10^{-8} \text{ m}^{-1} \text{ s}^{-1}$. The thick curve corresponds to the $q = 2.2 \times 10^{-8} \text{ m}^{-1} \text{ s}^{-1}$ contour. (b) Terms on the right-hand side of Eq. (10) for $q = 2.2 \times 10^{-8} \text{ m}^{-1} \text{ s}^{-1}$ contour: diabatic flux (thick light curve), hyperdiffusive flux (thick dark curve), and source within contour (thin curve). (c) Total cross-PV contour mass flux. A 15-day smoothing has been applied to fields in (b) and (c).

unshaded periods correspond to stages when there is growth of the vortex.

The hyperdiffusive mass flux is the result of sporadic transport of high PV out from the main vortex by Rossby wave breaking and the subsequent cascade to small scales by large-scale stirring. The filamentary structures produced by the wave breaking and stirring are eventually dissipated by the hyperdiffusion. Hence, during stages when the hyperdiffusive flux dominates the balance, there are fine-scale filamentary PV structures (see, e.g., day 75 in Fig. 6). In contrast, the diabatic mass flux is the result of the larger-scale height relaxation, which tends to increase the PV in polar regions and form zonally symmetric PV contours. During the stages

when the diabatic forcing dominates, there are very few small-scale PV anomalies and large scaler features are building in polar region (see, e.g., day 90 in Fig. 6).

The processes producing the two fluxes operate on different time scales. The filamentary transport out of the vortex occurs over a vortex turnover time (several days), whereas the radiative buildup occurs over the longer relaxation time scale. As a result the mass flux varies more rapidly during periods when the hyperdiffusive mass flux dominates; that is, compare the shaded region in Fig. 5c with nonshaded regions.

The general features of each of the vortex breakdown-recovery cycles shown in Fig. 5 are similar, but there are differences in the duration of the weak/no vor-

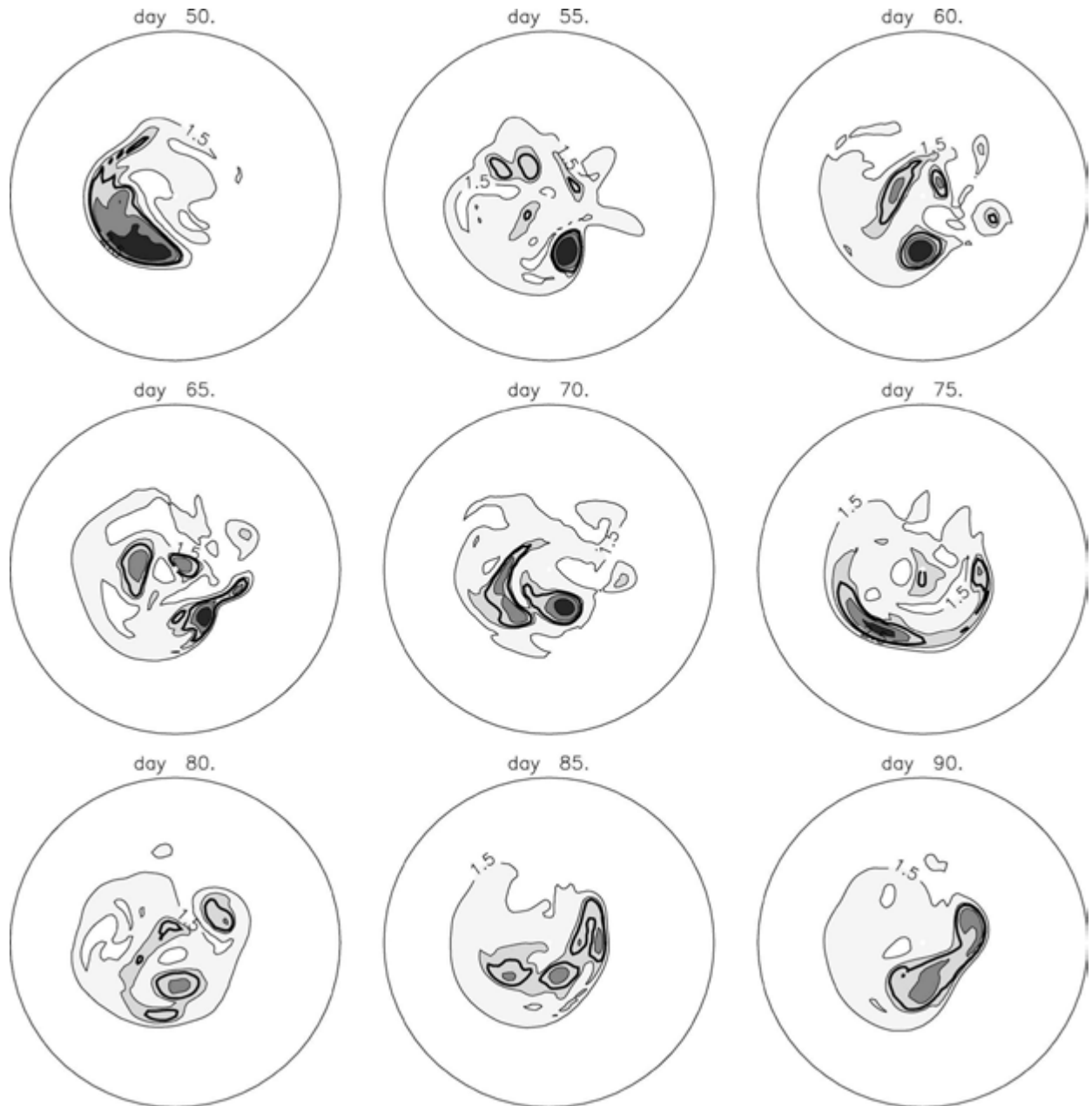


FIG. 6. As in Fig. 3c except for days 50 to 90: PV contours shown for $q = 1.5, 2.0, 2.2, 2.5,$ and $3.0 (\times 10^{-8} \text{ m}^{-1} \text{ s}^{-1})$ with $2.2 \times 10^{-8} \text{ m}^{-1} \text{ s}^{-1}$ contour in bold.

tex period. Examination of PV maps during these periods shows that these differences are related to the existence and evolution of small, coherent vortex remnants. When the main vortex breaks up, the region of high PV is not totally destroyed; rather small coherent remnants survive, for example Fig. 6. These remnants are greatly disturbed by the forcing and also interact with each other, but can persist for over 30 days. The persistence of these remnants appears to delay the re-

covery of the vortex, with rapid rebuilding of the vortex (over 10–15 days) occurring when the remnants are sheared out and destroyed.

Although vortex breakdown–recovery cycles occur regularly through the first 400 days of the $H_B = 3000$ m calculation, this is not the case for longer times. As shown in Fig. 7, a strong, robust vortex with high central PV develops around days 400 to 500, and the vortex vacillations stop. The exact cause for this is not known,

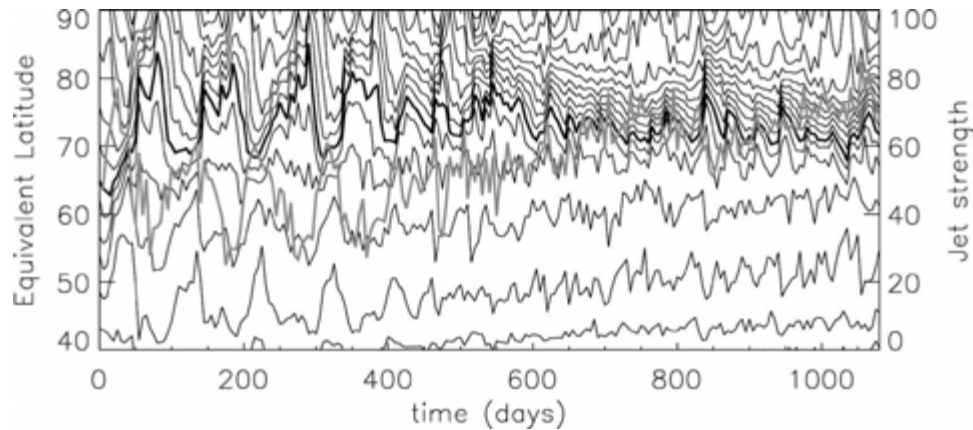


FIG. 7. As in Fig. 2f except for 1100 days.

but could be related to spurious effects due to the hyperdiffusion. Previous studies of two-dimensional vortex flows have shown that hyperdiffusivity induces spurious convergences near regions of high vorticity gradients at the edge of a vortex, which pump vorticity across the edge and increase the peak vorticity values at the center of the vortex (Mariotti et al. 1994; Yao et al. 1995). A similar increase of PV at the center of the vortex is seen in our calculations, and this may be the cause of the development of a very strong vortex that can resist the wave forcing and does not break down.

4. Sensitivity experiments

Above, we examined the vortex evolution for varying H_B with $\tau_E = 10$ days and focused on the large amplitude limit for which polar vortex vacillations occur. We now briefly describe the sensitivity of the vortex evolution, in this large H_B limit, to different aspects of the calculations. In particular, we examine under what conditions vortex breakdown–recovery vacillations occur.

The sensitivity to the initial flow conditions is examined by performing calculations with $H_B = 3000$ m and $\tau_E = 10$ days, but different initial conditions. Although the details of the flow vary with initial vortices, vacillations still occur for the different initial vortices. In particular, vacillations occur when the vortex is spun up from no initial flow (not shown).

There is, however, larger sensitivity to the relaxation time τ_E . Although vacillations occur for $H_B = 3000$ m and $\tau_E = 10$ or 15 days (not shown), they do not occur for this amplitude forcing and $\tau_E = 5$ or 20 days. As shown in Figs. 8a and 8c, when $\tau_E = 20$ days the vortex is initially destroyed and does not rebuild, whereas when $\tau_E = 5$ days the vortex does not break up. These different vortex evolutions can be understood in terms of the change in the balance between the diabatic and hyperdiffusive mass fluxes. While the time scale of variations in, and magnitude of, the hyperdiffusive fluxes are sim-

ilar for all values of τ_E , this is not the case for the diabatic mass flux. For longer τ_E the diabatic mass flux is smaller and varies less rapidly than for smaller τ_E (see Figs. 8b,d). As a result the variation in the mass fluxes is dominated by the diabatic flux for short τ_E , and the vortex does not break down. In the other limit the diabatic fluxes are weak and the vortex does not recover from the initial destruction of the vortex.

Note that, although the vortex area is approximately constant in both the $\tau_E = 5$ days and $H_B = 3000$ m calculation and the $\tau_E = 10$ days and $H_B = 1500$ m calculation shown earlier, the MLM balance is very different in the two calculations. In the small H_B , long τ_E case the vortex is approximately in steady state with only small deformations and is close to the equilibrium state, and the different mass flux terms are consistently small (not shown). This is in contrast to the large, rapidly varying fluxes shown in Fig. 8d.

When $H_B = 3000$ m, vacillations occur for τ_E equal to 10 and 15 days but not for $\tau_E = 5$ or 20 days. We have performed several additional calculations to examine the range of τ_E for which vortex breakup–recovery occur for smaller values of H_B . As $H_B = 3000$ m is insufficient to break up the vortex when $\tau_E = 5$ days, it follows that vortex breakup (and vacillations) do not occur for smaller values of H_B and $\tau_E = 5$ days. (We have not examined whether the vortex breaks up for larger H_B .) However it is possible that vortex breakup–recovery can occur for $\tau_E = 20$ days for smaller H_B . This is indeed the case for $H_B = 2500$ m, where vortex breakup–recovery cycles occurs for $10 \text{ days} \leq \tau_E \leq 20 \text{ days}$. For $H_B = 2000$ m the topographic forcing is too weak to break up for vortex, and vacillations occur only for $H_B > 2000$ m. The above calculations indicate that there is only a limited region of H_B – τ_E parameter space for which there is the right balance between relaxation and topographic forcing required for vortex breakdown–recovery cycles.

Returning to the $\tau_E = 10$ calculations, we now examine

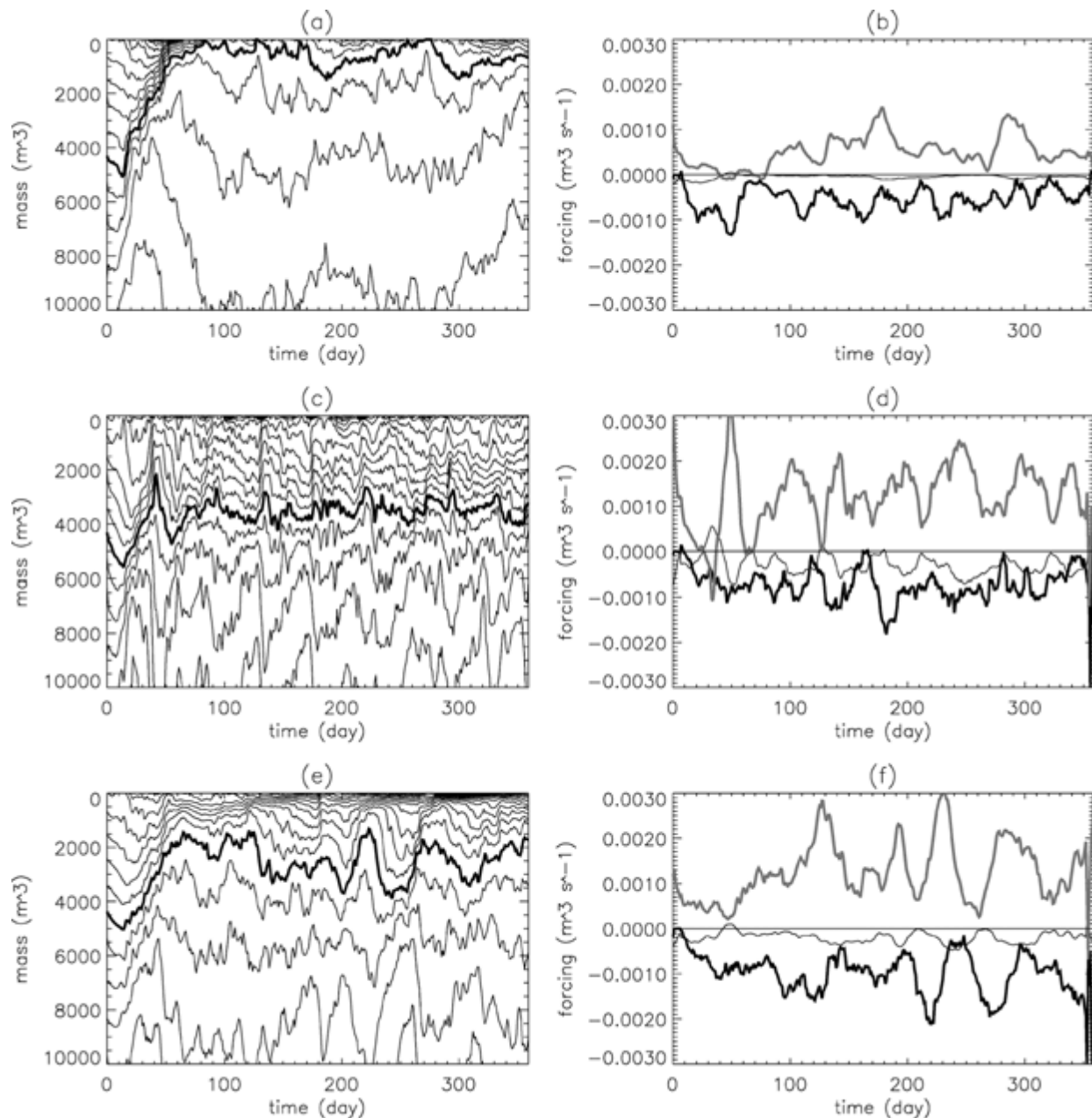


FIG. 8. Temporal evolution of the mass enclosed by PV contours and mass fluxes due to diabatic, hyperdiffusion for calculations with (a), (b) T42 resolution and $\tau_E = 20$ days; (c), (d) T42 resolution and $\tau_E = 5$ days; (e), (f) T85 resolution and $\tau_E = 10$ days; $H_B = 3000$ m in all calculations. Contour interval and line styles as in Fig. 5.

the impact of varying numerical resolution. The above calculations were performed at only modest spatial resolution (T42 and $\nu = 5 \times 10^{26} \text{ m}^6 \text{ s}^{-1}$) and it is important to verify the robustness of the results for higher resolutions. Figures 8e,f show the MLM budgets for a $H_B = 3000$ m calculation at T85 resolution and 50 times smaller hyperdiffusion coefficient ($\nu = 1 \times 10^{25} \text{ m}^6 \text{ s}^{-1}$). As in the T42 case (Fig. 5), cycles of vortex breakdown and

recovery can be seen. However, the cycles are more irregular and the complete shattering of the high PV is not seen. The details of the vortex cycles are therefore sensitive to the resolution.

Examination of PV maps (not shown) indicates that the weaker breakups and recovery in the higher-resolution calculation are due to the existence of stronger and more persistent vortex remnants. With the smaller

hyperdiffusion coefficient the vortex remnants diffuse less and, as discussed earlier, strong vortex remnants prevent the rebuilding of a large vortex and lead to a longer weak vortex stage. This is the case after the first breakup where vortex remnants produced during the breakup persisted for over 50 days, and the large area of high PV did not fully recover until day 120.

5. Concluding remarks

The calculations above demonstrate that internal modes of variability exist in a shallow-water model of the stratosphere. For large amplitude topographic forcing this internal variability is characterized by cycles of polar vortex destruction and recovery, with corresponding cycles of high-latitude westerlies and easterlies. These wind vacillations are reminiscent of those in models with multiple vertical levels (e.g., Holton and Mass 1976; Schoeberl and Strobel 1980; Yoden 1987; Christiansen 1999; Scott and Haynes 2000).

The vacillations in the shallow-water model are caused by out of phase variations in the mass fluxes across polar PV contours due to hyperdiffusion and those due to diabatic relaxation. The mass flux due to hyperdiffusion is largest during the breakup of the vortex, whereas the flux due to diabatic relaxation is largest during the vortex recovery. During the vortex breakup filamentary structures are produced and there is a cascade of PV to small scales, where it is eventually eliminated by hyperdiffusion (resulting in a decrease in mass with vortex PV contours). In contrast, during the vortex recovery there are few filamentary structures, and the mass flux is dominated by the increasing flux due to the diabatic relaxation.

These polar vortex vacillations can be understood in terms of variations in PV gradients and Rossby waves. When there is no vortex, there are weak gradients and hence weak Rossby waves, as PV gradients are required to sustain Rossby waves. As a result there is little disruption of the contours/flow, and the vortex strengthens under radiative effects. This strengthening leads to an increase in PV gradients, which allows Rossby waves to develop. When these Rossby waves reach sufficiently large amplitude, wave breaking occurs producing a cascade of PV to small scales and increasing PV gradients at the vortex edge. The wave breaking leads to the eventual destruction of the vortex (and PV gradients). Rossby wave activity, and in particular wave breaking, then decreases and the vortex rebuilds.

Although the discussion of vacillations in previous models with multiple vertical levels has focused on the transition from westerlies to easterlies and the development of critical lines, it is possible that some of these simulations may also be interpreted in terms of PV gradients. When there are strong westerlies, there are strong PV gradients at the edge of the polar vortex that favor upward propagation of Rossby waves. However, the formation of easterlies (in upper levels) implies weak PV

gradients and equatorward rather than upward wave propagation. The reduced wave activity in upper levels then allows the radiative recovery of the vortex.

The existence of polar vortex vacillations in a shallow-water model shows that the shielding of vertical propagation by easterlies is not a necessary element for vacillations. It also suggests that the horizontal flow structure may play an important role in the vortex breakdown and recovery in three-dimensional models and in the real stratosphere. Analysis of the vortex breakup and recovery in three-dimensional models and meteorological analyses from a PV perspective may provide insight into whether this is the case.

Acknowledgments. We thank Jessica Neu, Alan Plumb, Lorenzo Polvani, Richard Scott, and Darrell Strobel for helpful discussions and comments on earlier versions of the manuscript. This work was partially supported by NASA and NSF grants.

REFERENCES

- Andrews, D. G., J. R. Holton, and C. B. Leovy, 1987: *Middle Atmosphere Dynamics*. Academic Press, 489 pp.
- Baldwin, M. P., and T. J. Dunkerton, 1999: Downward propagation of the Arctic Oscillation from the stratosphere to the troposphere. *J. Geophys. Res.*, **104**, 30 937–30 946.
- and —, 2001: Stratospheric harbingers of anomalous weather regimes. *Science*, **294**, 581–584.
- Christiansen, B., 1999: Stratospheric vacillations in a general circulation model. *J. Atmos. Sci.*, **56**, 1858–1872.
- Holton, J. R., and C. Mass, 1976: Stratospheric vacillation cycles. *J. Atmos. Sci.*, **33**, 2218–2225.
- Juckes, M. N., 1989: A shallow water model of the winter stratosphere. *J. Atmos. Sci.*, **46**, 2934–2954.
- and M. E. McIntyre, 1987: A high-resolution one-layer model of breaking planetary waves in the stratosphere. *Nature*, **328**, 590–596.
- Mariotti, A., B. Legras, and D. G. Dritschel, 1994: Vortex stripping and the erosion of coherent structures in two-dimensional flows. *Phys. Fluids*, **6**, 3954–3962.
- Neu, J. L., 2002: Tropical transport and the seasonal variability of the subtropical “edges” in the stratosphere. Ph.D. thesis, Dept. of Earth, Atmospheric, and Planetary Sciences, Massachusetts Institute of Technology, 223 pp.
- Norton, W. A., 1994: Breaking Rossby waves in a model stratosphere diagnosed by a vortex-following coordinate system and a contour advection technique. *J. Atmos. Sci.*, **51**, 654–673.
- O’Sullivan, D., and M. L. Salby, 1990: Coupling of the quasi-biennial oscillation and the extratropical circulation in the stratosphere through planetary wave transport. *J. Atmos. Sci.*, **47**, 650–673.
- Polvani, L. M., D. W. Waugh, and R. A. Plumb, 1995: On the subtropical edge of the stratospheric surface zone. *J. Atmos. Sci.*, **52**, 1288–1309.
- Salby, M. L., R. R. Garcia, D. O’Sullivan, and J. Tribbia, 1990: Global transport calculations with an equivalent barotropic system. *J. Atmos. Sci.*, **47**, 188–214.
- Schoeberl, M. R., and D. F. Strobel, 1980: Numerical simulation of sudden stratospheric warmings. *J. Atmos. Sci.*, **37**, 214–236.
- Scott, R. K., and P. H. Haynes, 2000: Internal vacillations in stratospheric-only models. *J. Atmos. Sci.*, **57**, 3233–3250.
- Sobel, A. H., and R. A. Plumb, 1999: Quantitative diagnostics of mixing in a shallow-water model of the stratosphere. *J. Atmos. Sci.*, **56**, 2811–2929.

- Thompson, D. W. J., and J. M. Wallace, 1998: The Arctic oscillation signature in the wintertime geopotential height and temperature fields. *Geophys. Res. Lett.*, **25**, 1297–1300.
- , M. P. Baldwin, and J. M. Wallace, 2002: Stratospheric connection to Northern Hemisphere wintertime weather: Implications for prediction. *J. Climate*, **15**, 1421–1428.
- Thuburn, J., and V. Lagneau, 1999: Eulerian mean, contour integral, and finite-amplitude wave activity diagnostics applied to a single-layer model of the winter stratosphere. *J. Atmos. Sci.*, **56**, 689–710.
- Waugh, D. W., 1993: Contour Surgery simulations of a forced polar vortex. *J. Atmos. Sci.*, **50**, 714–730.
- Yao, H. B., N. J. Zabusky, and D. J. Dritschel, 1995: High-gradient phenomena in 2-dimensional vortex interactions. *Phys. Fluids*, **7**, 539–548.
- Yoden, S., 1987: Bifurcation properties of a stratospheric vacillation model. *J. Atmos. Sci.*, **44**, 1723–1733.
- , and K. Ishioka, 1993: A numerical experiment on the breakdown of a polar vortex due to forced Rossby waves. *J. Meteor. Soc. Japan*, **71**, 59–72.